PERGAMON

International Journal of Solids and Structures 40 (2003) 591–610

INTERNATIONAL JOURNAL OF SOLIDS and STRUCTURES

www.elsevier.com/locate/ijsolstr

Fracture mechanics analysis of thin coatings under plane-strain indentation

Herzl Chai *

Department of Solid Mechanics, Materials and Systems, Faculty of Engineering, Tel Aviv University, Tel Aviv 69978, Israel

Received 5 April 2002; received in revised form 10 October 2002

Abstract

A combined experimental/analytical work is carried out to elucidate the fracture resistance of a thin, hard coating bonded to a semi-infinite substrate due to indentation by a cylindrical surface. The bending of the coating under the softer substrate induces concentrated tensile stress regions at the lower and upper surfaces of the coating, from which cracks may ensue. The evolution of such damage in a model transparent system (glass/polycarbonate) is viewed in situ from below and from the side of the specimen. The critical load needed to initiate a crack on the lower coating surface generally increase proportionally to the coatings thickness, d. An interesting departure from this trend occurs for thin coatings, where the fracture load, although marred by a large scatter, *increases* somewhat with decreasing d. The fracture data for the upper coating surface are limited to relatively thick coatings due to the recurrence of premature failure from the coating edges. The behavior in this range is similar to that for the lower surface crack, albeit with an order of magnitude greater fracture resistance.

A fracture mechanics analysis in conjunction with FEM is performed to elucidate the stress intensity factors responsible for crack propagation. A crack normal to the coating surface is assumed to emanate either from the lower or upper surface of the coating. A major feature of the solution is the occurrence of a bending-induced compression stress field over a region ahead of the crack tip. This effect, which become more dominant as the ratio between the contact length and the coating thickness is increased, tends to delay the onset of crack propagation, especially for the lower surface crack. Consequently, in applications associated with large indenters, thin and/or tough coatings and stiff substrates, cracking from the upper coating surface may *precede* that from the lower surface. An interesting feature of this crack shielding mechanism is that when the coating surface contains a *distribution* of flaws rather than a single crack, small flaws in this population may be more detrimental than large ones. Incorporation of these aspects into the analysis leads to a good correlation with the test results. In the special case of *line loading*, which constitutes a *lower bound* for the critical loads, a closed-form, approximate solution for the stress intensity factors or the critical loads are obtained.

Plane-strain indentation, although less common than spherical indentation, allows for characterizing the fracture resistance of opaque films through observation from the specimen edge. This approach is not easily implemented to thin films (i.e., less than about a hundred microns), however.

Keywords: Indentation; Coating; Crack; Plane-strain

* Fax: +972-3-6407617.
E-mail address: herzl@eng.tau.ac.il (H. Chai).

0020-7683/02/$ - see front matter © 2002 Elsevier Science Ltd. All rights reserved.
PII: S0020-7683(02)00619-4

1. Introduction

The resistance of layered structures to contact damage is of interest in variety of industrial and technological applications, including tribology, bioengineering and electronic packaging devices. Beyond damage tolerance concerns, indentation may also serve as a simple and efficient mean for characterizing the strength and stiffness of hard materials (Lawn et al., 2000). While the damage tolerance of such systems is affected by a variety of material and geometric parameters, we focus on thin, hard coatings and compliant substrates. The bending of the coating over the softer foundation induces concentrated tensile stresses at the bottom and upper surfaces of the coating, from which cracks may ensue. In the analysis of such damage, it is convenient to distinguish between small and large coating thickness. In the latter case, a fracture mechanics criterion based on the critical surface stress, σ_F, was found to work well for laminated window glass (e.g., Lardner et al., 1997; Chai et al., 1999) as well as a variety of ceramics (Rhee et al., 2001). When the thickness of the coating is comparable to the contact length or the length of the crack present on the specimen surface, a significant departure from this stress criterion occurs (Chai et al., 1999). Under these circumstances, a fracture mechanics approach incorporating the full contact problem would be necessary. It is this issue that is of concern in the present investigation. Although spherical indentation is widely used for probing the fracture resistance of thin, brittle coating films (e.g., Diao et al., 1994; Weppelmann and Swain, 1996; Wang et al., 1998; Michler et al., 1999; Yuan and Hayashi, 1999; Souza et al., 2001; Abdul-Baqi and Van der Giessen, 2002), this approach has some serious limitations when applied to opaque materials. In this case, the analysis is necessarily limited to fracture that originates from the free surface of the coating, the latter that is generally observed *after the fact*. Moreover, the fracture at the lower coating surface, which is often more dominating, is difficult to quantify experimentally and analytically, the latter difficulty stemming from the three-dimensional nature of the fracture problem.

Recently, Chai et al. (1999) employed an all-transparent bi-layer system consisting of a glass layer bonded to a thick polycarbonate slab, the whole of which is indented by a nearly rigid sphere. Glass serves as an ideal brittle material. Moreover, by pre-abrading its surface with slurry of fine particles, the scatter in the fracture data is greatly reduced. By employing in situ observations from below and from the side of the samples, valuable insight into the evolution and growth of damage in both the lower and upper surfaces of the coating was gained. Extension of this approach to plane-strain indentation is appealing in that it offers an important simplification in the fracture analysis of the lower coating surface, i.e., from a 3-D to a 2-D configuration. Moreover, the ability to observe the fracture process from the specimen side allows this method to be applied also to opaque materials. (To realize this benefit, however, one must first overcome common technical obstacles such as the occurrence of premature fracture or chipping from the specimen edges.) Beyond these considerations, the subject of plane-strain indentation is of direct interest in a variety of technological applications associated with rolling contact (e.g., Goryacheva and Sadeghi, 1995; Benabdallah and Boros, 1996; Gilpin et al., 1996; Mahajan, 1998; Elsharkawy, 1999).

In this work, a combined experimental/analytical effort is carried out to elucidate the response of thin-coating structures to plane-strain indentation. Tests are carried out on glass/polycarbonate bi-layers subject to indentation by a steel cylinder of radius $r = 3$ mm. The systems of cracks observed in these tests are depicted in Fig. 1. As shown, cracks may emanate either from the lower or the upper surfaces of the coating. (Depending on the problem parameters, the crack on the lower coating surface may occur on the symmetry plane or a certain distance away from it.) Critical loads to initiate such cracks are evaluated as a function of the coating thickness, d. A fracture mechanics based finite element analysis (FEA) is carried out to evaluate the critical loads for crack propagation and the effect of the various geometric and material parameters involved. The experiments are reported in Section 2 while the FEA is given in Sections 3 and 4. The fundamental case of line-load (i.e., $r \to 0$) is analyzed first (Section 3). Results for a finite indenter radius (i.e., 3 mm), mostly limited to the test conditions, are given in Section 4. The analyses are first performed for an uncracked coating in order to provide a database for the fracture analysis. The

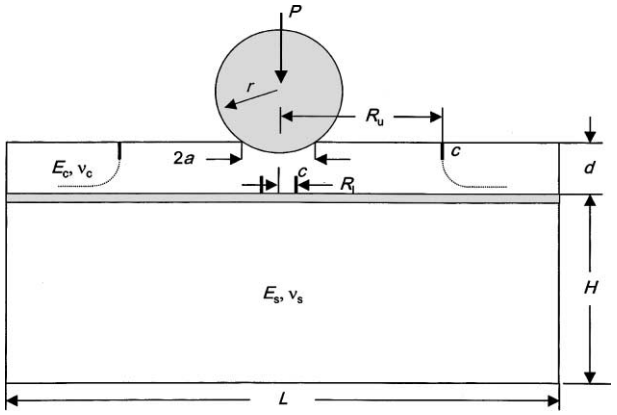

Fig. 1. Crack system in a thin coating bonded to a thick substrate due to indentation by a cylindrical surface. Note that under certain conditions, the crack on the lower coating surface may occur *away* from the symmetry plane, and that on the upper coating surface may propagate *toward* the symmetry plane.

relationship between the critical stress criterion and the fracture mechanics approach is discussed in Section 5.

2. Experimental

2.1. Apparatus

The present testing approach is much similar to that used in the spherical indentation tests (Chai et al., 1999). The specimens (Fig. 1) are fabricated from soda-lime microscope glass plates (Young's modulus, E_c equals 70 GPa and Poisson's ratio, ν_c, equals 0.22), which are bonded to a 12.5 mm thick, clear polycarbonate block ($E_s = 2.35$ GPa, $\nu_s = 0.35$) by means of a thin (<10 μm) epoxy adhesive (Harcos Chemicals, Bellesville, NJ) having similar elastic properties to those of the substrate. The dimensions of the cover layer are 25 mm × 75 mm × d, where d is the coating thickness. Coatings of different thickness are produced from the glass slides by means of polishing or, in the case of very thin coatings, by etching in a 10% concentration hydrofluoric acid solution for various durations. The top or bottom surface of the glass is pre-abraded with slurry of 600 Sic grit. This produces flaws from which cracks may initiate in a controlled and repeatable manner. The opposing glass surface is etched in hydrofluoric acid to minimize unwanted cracks. The indenter is a tool steel cylinder ($E_i = 210$ GPa, $\nu_i = 0.22$) of radius $r = 3$ mm and a length coincident with the specimen width (i.e., 25 mm). Initial tests were marred by the occurrence of premature chipping failure that has originated from the edges of the specimen. To reduce this effect, a double-cross loading arrangement is used.

Indentations are made at a slow crosshead speed such that fracture occurs within 10–30 s. The evolution of damage in the glass is generally observed from below, through the substrate. To enhance reflectivity, a thin film of gold is evaporated on the indented surface of the coating. To examine the feasibility of applying this test concept to opaque materials, some samples are also viewed from the side, with the specimen edge first polished and then coated with a film of gold. The fracture process is observed in-situ using a video camera that is connected to a zoom telescope (Questar). Critical loads to initiate fracture in the lower or upper surfaces of the coating are measured as a function of the coating thickness.

2.2. Test results

Referring to Fig. 1 for notation, cracks in the present tests occurred either on the lower surface of the glass, directly under the indenter (i.e., $R_i = 0$), or on the upper surface, a certain distance R_u from the contact plane. No delaminations are observed in the tests, attesting to the good bonding between the coating and the substrate. Fig. 2 shows several micrographs exemplifying the damage evolution on the lower coating surface as observed from the side (a) and from below the sample (b). In these tests the lower surface of the coating was abraded while the upper one chemically etched. Each of the prints in Fig. 2 except print II in (a) correspond to just after the formation of the crack. As indicated from frame I of the side view, the crack initiates from the lower surface of the glass, right under the indenter. The crack grew in the vertical direction, initially extending to approximately three-quarters of the glass thickness. Upon increasing the load by about 20% (print II), the crack extends nearly all the way to the top surface of the glass. When observed from below the sample, Fig. 2b, the cracks generally appear as straight lines, co-linear with the axis of the indenter. In some tests, particularly those with relatively large coating thickness, a broom like fracture pattern was also observed (print II of Fig. 2b). Typical side view results are shown in Fig. 3; for both the cases shown, the lower coating surface was etched while the upper one abraded. Consider first print (a). Following an early cracking on the bottom surface of the coating, two nearly symmetric cracks emerge from the upper coating surface, several coating thickness away from the symmetry plane. These cracks have occurred nearly simultaneously, at about the load level indicated in the print. The cracks first extend downward before turning away from the symmetry plane, where they continued to grow laterally, fairly close to the interface. The fracture behavior in Fig. 3b is similar to that just described, except that the crack now grow *toward* the plane of symmetry. (A close examination reveals the existence of yet another, smaller crack, that grew in the opposite direction.) Inward growing cracks were generally associated with a bit larger relative distance R_u/d than outward growing cracks. A possible explanation for these different crack paths is given in Section 4.3, following the development of the nonlinear FEA.

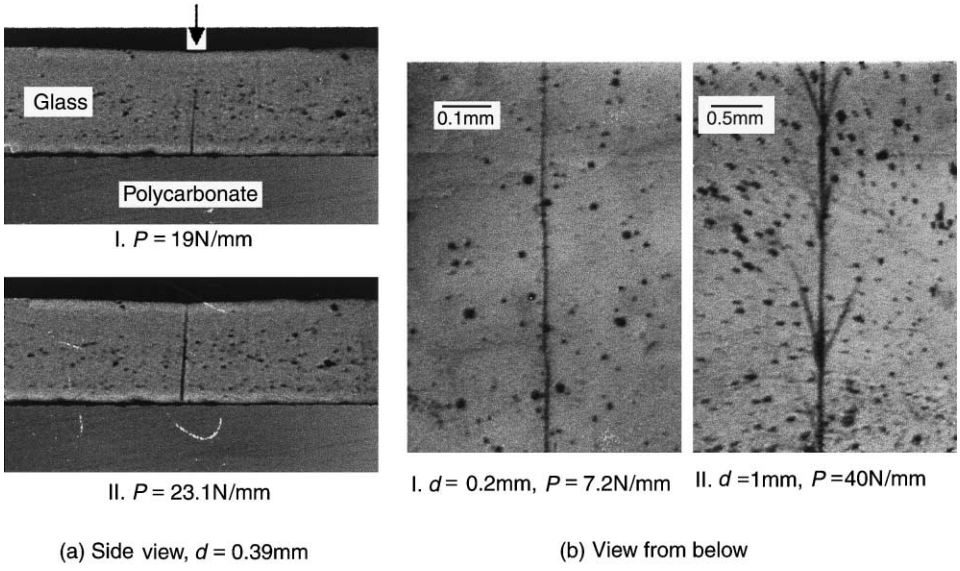

Fig. 2. Evolution of damage in a glass/polycarbonate bi-layer in which the lower coating surface is abraded while the upper one is etched; indenter is a steel cylinder of radius $r = 3$ mm: (a) views from the specimen side, with the sides first polished and then coated with a thin layer of gold and (b) views from below the specimen. Note that all the micrographs except II in (a) correspond to just after the onset of damage. Note also that only part of the structure is shown in these prints.

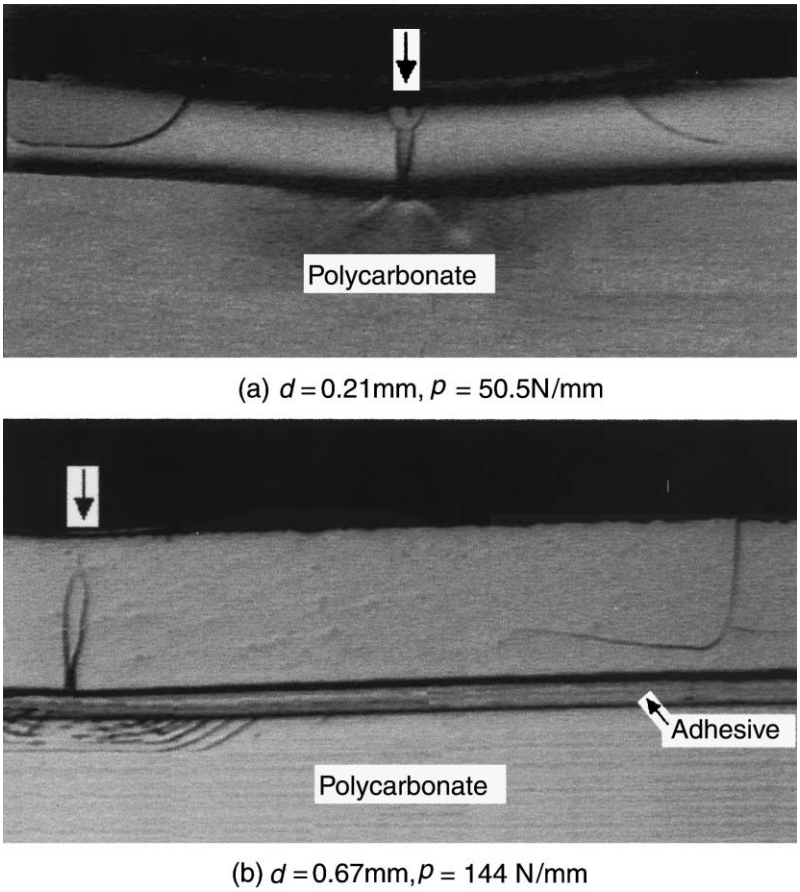

Fig. 3. Evolution of damage in a glass/polycarbonate bi-layer in which the upper coating surface is abraded; the indenter is a 3 mm radius steel cylinder. The damage was recorded from the specimen side, with the latter polished and then coated with a thin layer of gold: (a) $d = 0.21$ mm and (b) $d = 0.67$ mm. Each micrograph corresponds to just after the onset of damage at the upper coating surface. Note that in each of these prints, the crack on the lower coating surface occurred earlier than that on the upper coating surface, despite the fact that the former was etched prior to bonding. Note also that in the case of (b), only the right-hand side of the specimen is illustrated. Note that the dark bands between the coating and the adhesive are artifact, not delamination.

The dependence of the critical loads (on a per unit length basis) needed to cause crack propagation, P_{cr}, on the coating thickness is given in Fig. 4, [1] where the filled and open symbols represent the lower and upper coating surfaces, respectively. Circles and triangles in this figure correspond to observations from below and from the side of the specimens, respectively. The data from these two approaches seem quite similar. Before commenting further on these results, we note the large scatter that accompanies the data, the effect that tend to increase with decreasing d. In fact, for the upper surface crack, no viable data could be generated once d was decreased from about 200 μm. This scatter, which tended to occur in repeatable tests, is attributed to misalignments in the loading apparatus. Nevertheless, the trends seem quite clear. For thick coatings, the critical loads seem to decrease linearly with decreasing the coating thickness, with the critical

[1] Some of the data in this figure, specifically those pertaining to relatively large coating thickness, were scaled with the aid of the FEA such that they would represent half-space support conditions. The details are deferred to Section 3.1.

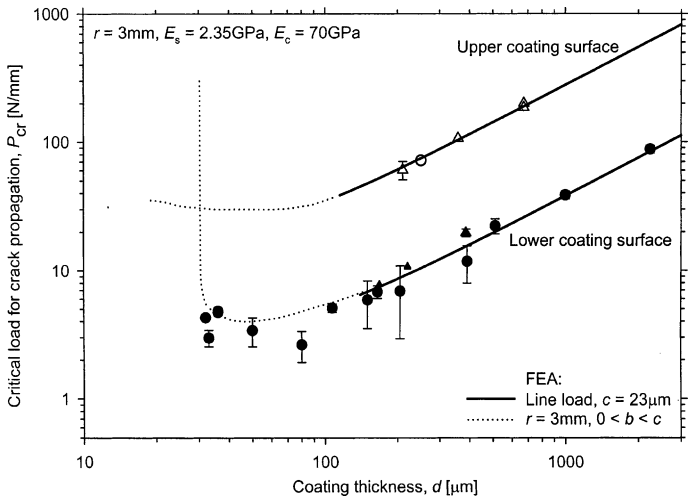

Fig. 4. Critical loads for crack propagation in a glass/polycarbonate system indented by a steel cylinder of radius $r = 3$ mm. Filled and open symbols are experimental data (mean and standard deviation) associated with the lower and upper surface cracks, respectively; circles and triangular symbols correspond to observations from below and from the side of the specimens, respectively. Curves denote FEA predictions, with the solid and the dotted lines corresponding, respectively, to the line-load analysis, based on a 23 μm long crack, and the nonlinear (i.e., $r = 3$ mm) analysis, based on a flaw distribution in the range $0 < b < 23$ μm.

load for the upper surface crack being about ten times greater than its lower surface counterpart. For relatively thin coatings (e.g., <100 μm), a change in trends occurs, with the fracture strength (in the case of the lower surface crack) slightly *increasing* with decreasing d. The general behavior observed in these tests is much similar to that for the axisymmetric analogue (Chai et al., 1999). A noticeable difference between these two configurations is the proportionality of P_{cr} to d here as opposed to d^2 in the axisymmetric case.

In the followings, a fracture mechanics approach is developed in order to predict the dependence of the critical loads on the various geometric and material parameters of the problem. Special emphasis is given to thin coatings, where the strength unexpectedly increases with decreasing the coating thickness. It should be noted that Miranda et al. (2001) has considered this phenomenon in connection with the axisymmetric bi-layer configuration. It was proposed in this work that such strengthening effect, in the case of the lower surface crack, is attributable to the existence of distributions in flaw size and location, in relation to the bell-shaped tensile stress field on the lower coating surface. This consideration led to a certain increase in the fracture resistance.

3. Finite element analysis—line loading

A commercial finite element code (ANSYS, Version 5.7), specified to plane-strain conditions, is used for evaluating the stress distributions in the bi-layer structure due to indentation by a steel cylinder. In this section, the radius of the indenter is taken to be sufficiently small so as to simulate line-load conditions. (Treatment of a finite size indenter is deferred to Section 4.) The line-load analysis is useful in that it leads to a linear relation between load and stresses at any point in the structure (provided that none of the constituents undergoes inelastic deformation) and, as will be discussed latter, it also provides lower bounds for the fracture loads. In addition, this analysis becomes directly applicable when the coating thickness is large relative to the contact length, $2a$. A small load ($P = 0.1$ N/mm) is applied so as to exclude possible geometric or material nonlinearities. The interface is assumed well bonded as no delaminations are observed in

the tests. A preliminary study showed that the vertical and horizontal dimensions of the substrate must be at least 150 and 300 times the coating thickness, respectively, in order to simulate a half-space support. These dimensions are thus used throughout this work. Analyses are first performed for uncracked coatings, from which useful empirical relations for the variations of the radial stress responsible for crack propagation with the coating thickness and elastic moduli are obtained. Next, FEA are performed for bi-layers containing a vertical crack of length c, which may emanate either from the lower or upper surfaces of the coating (Fig. 1). A fine mesh in the regions of stress concentration is used. The mesh is refined until convergence is attained. To take advantage of symmetry, only half of the structure is treated.

3.1. Stress analysis—no crack

Fig. 5a shows contours of radial (i.e., the lateral direction) stress for a thin glass coating ($d = 20$ μm) bonded to a polycarbonate substrate at increasing load levels; only the coating part is illustrated in the figure. To help distinguish between tensile and compression stresses, the contour lines for the latter are drawn with low contrast. Consider at this time only the first print, where, by virtue of the smallness of the load (i.e., $P = 0.1$ N/mm), the results are representative of the line-load case (even though the indenter radius (i.e., 3 mm) is finite). Two regions of stress concentration are apparent, one on the lower surface, directly under the indenter, and the other on the top surface of the coating, several coating thickness away from the symmetry axis. The stress distribution across the coating in these regions resembles that for plate bending, with the neutral axis occurring near the mid-plane of the coating layer. The compression stress field in these regions would hinder crack propagation, especially for relatively large cracks where the crack tip may lie inside the compression zone. This interesting feature is discussed in Section 3.2. In the following subsection, quantitative information on the peak radial stresses, where cracking may initiate, is sought.

Fig. 6 (filled symbols) shows the dependence of the peak radial stress at the lower and upper surfaces of the coating, σ_l and σ_u, respectively, on the coating thickness for a given materials choice (i.e., glass bonded to polycarbonate). These data were generated using $d = 1$ mm and $P = 0.1$ N/mm. As shown, both σ_l and σ_u are inversely proportional to d throughout the thickness range. (This is in line with the $1/\rho$ type stress decay characterizing the monolith configuration, where ρ is the distance from the loading plane (e.g., Johnson, 1996).) One also observes that the stress on the lower coating surface is about an order of

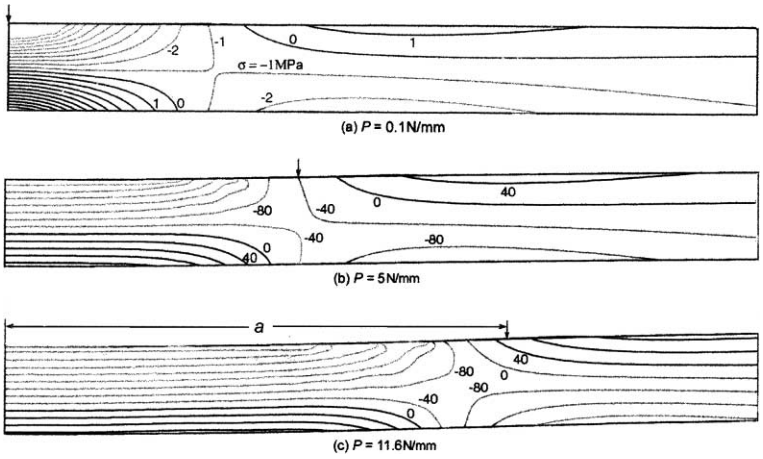

Fig. 5. FEM radial stress contours in the coating region for a glass/polycarbonate system at increasing load levels; $d = 20$ μm, indenter is a steel cylinder of radius $r = 3$ mm. Low and high contrast contours denote negative and positive stresses, respectively. Vertical arrows indicate the extent of contact.

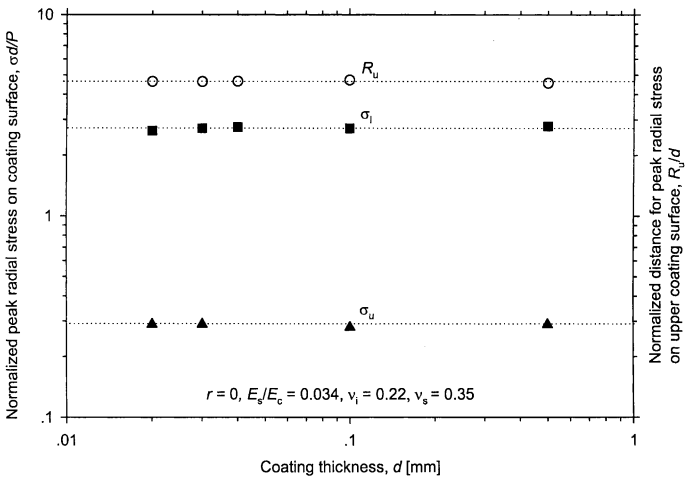

Fig. 6. FEM predictions for the variations with coating thickness of the normalized position of the peak radial stress on the top surface of the coating (circles), the normalized radial stress there (triangular symbols), and the normalized radial stress on the lower coating surface, right on the symmetry plane (rectangular symbols); a glass/polycarbonate bi-layer subject to line-load. Dotted lines are fits to the data.

magnitude greater than that for the upper surface. Also shown in this figure is the dependence of R_u, the distance from the symmetry plane to the peak radial stress on the upper coating surface, on d. As shown, R_u is proportional to d throughout the thickness range. One may thus write

$$\sigma_l = f_l P/d, \quad \sigma_u = f_u P/d, \quad R_u = f_R d, \tag{1}$$

where f_l, f_u and f_R are some functions of the modulus mismatch E_s/E_c (and possibly of other material and geometric parameters), being equal to 2.75, 0.29 and 4.6, in that order, in the case of the glass/polycarbonate bi-layer. For relatively thick coatings (i.e., $d \gg c$, where c is the crack length), the critical loads for crack propagation can be directly obtained from these relations by substituting a critical value, σ_F, for these stresses (Chai et al., 1999).

A side study was conducted to determine how the finite dimensions of the substrate used in the tests are related to the critical loads that would be obtained had the substrate been infinitely large. Table 1 compares FEM generated peak stress values corresponding to the experiments (i.e., $H = 12.5$ mm, $L = 10$ mm; the latter dimension correspond to the distance between two neighboring indentation sites in the tests) with those for the simulated half-space support ($H = 150d$, $L = 300d$). The results, corresponding to a number of representative tests, show that the size effect, expressed as the ratio between the peak stress corresponding to the finite size and the infinitely thick substrates, F, seem to be significant only for the upper surface cracks, the more so with increasing d. The stress ratios obtained in this way were used to scale the experimental results given in Fig. 4.

Table 1
Scaling factors (F_u and F_l) for experimentally obtained fracture loads[a]

d (μm)	h (mm)	L (mm)	$\sigma_l d/P$	$\sigma_u d/P$	F_l	F_u
0.188	12.5	10	2.79	0.327	1.03	1.13
0.357	12.5	10	2.82	0.357	1.04	1.23
0.672	12.5	10	2.86	0.403	1.06	1.39

[a] Results pertain to glass/polycarbonate bi-layer. For infinitely thick substrate, the FEA gives $\sigma_l d/P = 2.7$, $\sigma_u d/P = 0.29$.

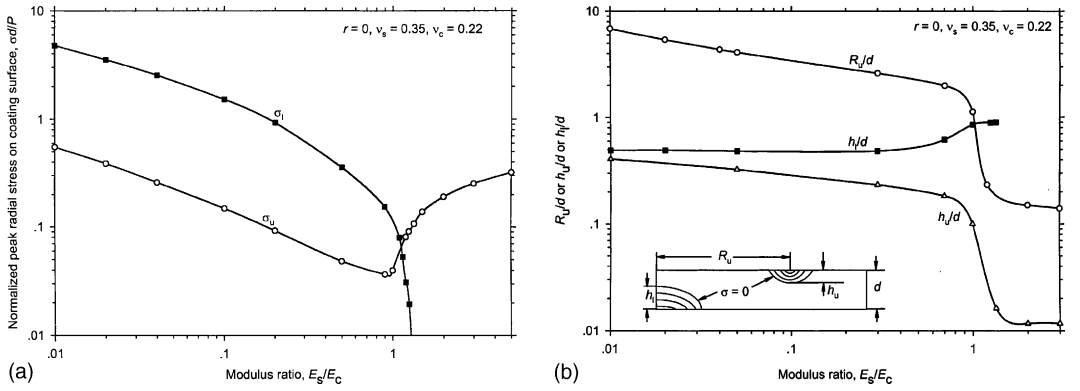

Fig. 7. Line-load FEM predictions (symbols) for the variations with substrate/coating modulus ratio of the normalized peak radial stress on the lower and upper coating surfaces (a), and associated geometric quantities (b). Solid lines are smooth fits to the data.

The functions f in Eq. (1) may be determined from Fig. 7a, which shows the effect of the modulus ratio on the peak radial stresses. The peak stress on the lower surface monotonically decreases with increasing the substrate stiffness, becoming negative when E_s/E_c is increased from 1.3. The behavior for the upper surface follows a similar trend up to a modulus ratio of about unity. When the substrate becomes stiffer than the coating, however, a major departure occurs, with σ_u increasing with E_s/E_c. This indicates that for relatively stiff substrates, the upper surface crack may become the detrimental strength factor for the bi-layer structure. Fig. 7b (open circles) shows the effect of the modulus ratio on the position of the peak radial stress on the upper coating surface, R_u. The latter monotonically decrease with increasing the substrate stiffness, incurring a dramatic reduction once the substrate stiffness exceeds that of the coating. In this range, the peak stress shifts to the vicinity of the edge of the contact axis. Also shown in this figure are the quantities h_l and h_u (see insert) which define the location of the neutral axis of the bent coating layer in the stress concentration regions. For a relatively soft substrate, both h_l/d and h_u/d tend to 0.5, in line with the behavior for a bent beam. When E_s/E_c approaches unity, the stress on the upper surface tends to concentrate on a narrow layer on the free surface. The behavior for the bottom surface in this range is more involved.

3.2. Crack analysis

Referring to Fig. 1, consider a vertical crack of length c, extending either upward from the lower coating surface, directly under the indenter (i.e., $R_l = 0$), or downward from the upper coating surface, a distance R_u from the symmetry plane, where the radial stress attains a peak value. The stress intensity factor for each of these crack systems is evaluated next. A similar problem was treated by Gecit (1979), except that the loading was applied in the plane of the coating, as opposed to the concentrated transverse load used here.

3.2.1. Stress intensity factors

For the lower surface crack (with $R_l = 0$), only mode I stress field exists. Let the stress intensity factor in this case be expressed as

$$K_I = \alpha\sigma_l\sqrt{\pi c} \tag{2}$$

where $\alpha = \alpha(c/d)$ is a correction over the Griffith crack case ($\alpha = 1$). This function is determined with the aid of the FEA as follows. Let u denote the crack opening displacement on the crack flank, a distance Δ behind the tip. LEFM then gives (e.g., Ewalds and Wanhill, 1986)

$$u = \frac{4(1-\nu_c^2)K_1\sqrt{\Delta/2\pi}}{E_c} \tag{3}$$

Making use of (1) and (2), one has

$$\alpha = \frac{\sqrt{2c/\Delta}(uE_c/P)(d/c)}{4(1-\nu_c^2)f_1} \tag{4}$$

FEA are performed for a number of bi-layer material choices and various values of d, all with $c = 0.03$ mm and $P = 0.1$ N/mm. A fine mesh consisting of uniform square grids having a cell size of 0.5 μm is implemented at the crack tip vicinity. The existence of a K-field solution is assessed by comparing the distribution of the opening displacement behind the crack tip with the near-tip theoretical $1/s^{0.5}$ type decay, where s denote the distance from the crack tip. For our choice of $\Delta = 0.5$ μm, this relationship is generally maintained to within 1–2%, except when c approaches d, where differences of up to several percents occur. Inserting the values of u at $s = \Delta$ from the FEA in Eq. (4), and using values for f_1 from the uncracked configuration, α could be determined for a given value of d. The results for various values of d and three choices of the modulus ratio E_s/E_c (i.e., 0.034, 0.2 and 0.5) are given in Fig. 8a (filled symbols). The effect of the modulus ratio seems moderate. In each case, the normalized stress intensity factor monotonically decreases from its asymptotic value at $c/d = 0$ (i.e., ≈0.8), drastically diminishing once the crack becomes about 70% of the coating thickness. For larger values of c/d, contact between the two crack faces occurs. The data in each case seem to be well fitted by a cubic polynomial (solid lines) which coefficients are given in Table 2.

For the upper surface crack, the fracture is mixed-mode. Let the mode I and mode II stress intensity factors in this case, K_1 and K_2, be similarly written as

$$K_i = \alpha_i \sigma_u \sqrt{\pi c}, \quad i = 1, 2 \tag{5}$$

where $\alpha_i = \alpha_i(c/d)$. Making use of the fracture mechanics relations

$$u_i = \frac{4(1-\nu_c^2)K_i\sqrt{\Delta/2\pi}}{E_c}, \quad i = 1, 2 \tag{6}$$

where u_1 and u_2 are the opening and shearing displacements behind the crack tip, respectively, one has from Eqs. (1), (5) and (6)

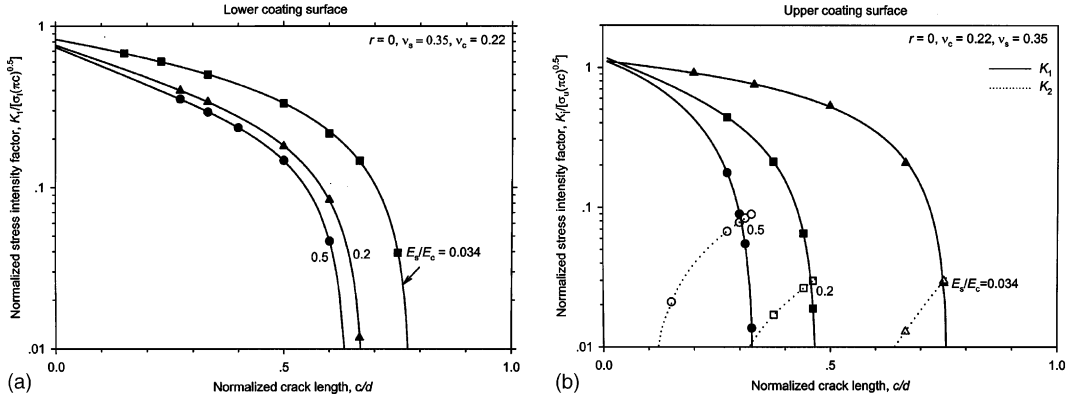

Fig. 8. Line-load FEM predictions (symbols) for the variations of normalized stress intensity factors with normalized crack length, for three coating/substrate modulus ratios: (a) lower coating surface and (b) upper coating surface. Curves are cubic polynomial fits, with coefficients given in Table 2. (Note that the data are limited to those c/d values for which no contact between the crack faces occurs.)

Table 2
Polynomial coefficients for the stress intensity factors in the line-load analysis[a]

Coating surface	K	E_s/E_c	a_0	a_1	a_2	a_3
Lower	K_1	0.034	0.8278	−1.0281	0.2912	−0.4275
	K_1	0.2	0.7608	−1.7017	1.7382	−1.3055
	K_1	0.5	0.7397	−1.9944	2.7011	−2.1698
Upper	K_1	0.034	1.1171	−0.9951	0.0634	−0.9030
	K_1	0.2	1.1943	−3.4767	3.4557	−3.1234
	K_1	0.5	1.1311	−3.0751	−3.9745	8.8964
	K_2	0.034	−0.1210	0.7855	−1.6580	1.1718
	K_2	0.2	−0.0639	0.4310	−0.9246	0.9333
	K_2	0.5	1.4805	−14.7716	50.2395	−55.2667

[a] $K/[\sigma(\pi c)^{0.5}] = a_0 + a_1(c/d)^1 + a_2(c/d)^2 + a_3(c/d)^3$.

$$\alpha_i = \frac{\sqrt{2c/\Delta}(u_i E_c/P)(d/c)}{4(1-\nu_c^2)f_u}, \quad i = 1,2 \tag{7}$$

The results for this case, obtained similarly to that for the lower surface crack, are shown in Fig. 8b as filled (K_1) and open (K_2) symbols, with the solid and dotted sets of lines corresponding to cubic polynomial fits which coefficients are given in Table 2. The mode I stress intensity factor behaves similarly to its lower surface counterpart (Fig. 8a), except for a much greater sensitivity to the modulus ratio. In contrast to K_1, the mode II component increases monotonically as the ratio c/d is increased. Because contact is excluded in the analysis, we shall limit the discussions in the following to the condition $K_1 > 0$ (even though fracture in the post contact regime may still occur through the mode II component).

3.2.2. Critical loads

The onset of crack propagation under general mixed mode conditions is assumed to occur when the energy release rate, G, equals its critical value, G_c, where

$$G = (K_1^2 + K_2^2)(1-\nu_c^2)/E_c \tag{8}$$

Making use of the preceding equations, the critical loads for crack propagation (over the range $K_1 > 0$) are found as

$$\text{Lower coating surface:} \quad P_{cr} = K_c d/[\alpha f_1 \sqrt{\pi c}] \tag{9}$$

$$\text{Upper coating surface:} \quad P_{cr} = K_c d \Big/ \left[f_u \sqrt{(\alpha_1^2 + \alpha_2^2)\pi c}\right] \tag{10}$$

where, for simplicity reason, we define

$$K_c \equiv \sqrt{E_c G_C/(1-\nu_c^2)} \tag{11}$$

Fig. 9a and b (solid lines) shows the variations with d/c of the normalized critical loads needed to initiate crack growth in the lower and upper coating surfaces, respectively. This presentation, specified to three choices of E_s/E_c, allows one to follow the variations of the critical loads with the coating thickness for a fixed crack length. Consider first, the case of a relatively soft substrate, i.e., $E_s/E_c = 0.034$. The behavior for the two crack systems is quite similar apart from about an order of magnitude difference in favor of the upper surface crack. For relatively thick coatings, the critical loads tend to increase linearly with d. As the ratio d/c decreases from about 10, a change in trends occurs, with the strength curves bending upward, tending to infinity as the coating thickness becomes comparable to the length of the crack. This rather

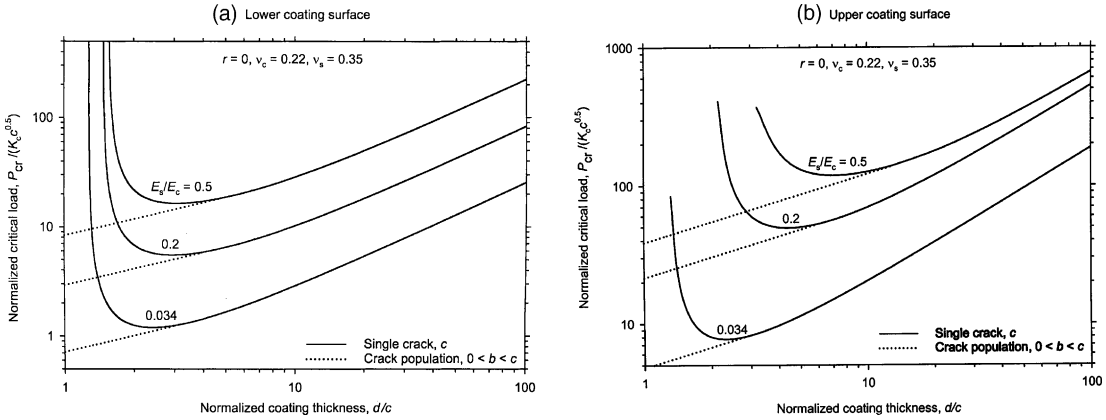

Fig. 9. FEM fracture mechanics predictions for the variations with normalized coating thickness of the normalized critical loads needed to initiate a crack on the lower (a) and upper (b) coating surfaces. The results, which pertain to the line-load analysis, are specified to three different coating/substrate modulus ratios. Solid curves pertain to a single crack of length c, dotted curves are predictions for a population of flaws in the range $0 < b < c$.

unique strengthening effect is a fundamental feature of indentation type loading. It can be seen from Fig. 9a and b that increasing the substrate stiffness tend to increase in the critical load as well as reduce the strength difference between the lower and upper surface cracks.

3.2.3. Crack stability

Next consider the crack growth history. Fig. 10 shows the variations of the normalized critical loads with the normalized crack length for the case $E_s/E_c = 0.034$. These curves are generated from Eqs. (9) and (10) using the values of f_l and f_u from Fig. 6 and the coefficients given in Table 2. This presentation allows one to follow the crack growth history for a fixed coating thickness. The curves for the two crack systems are

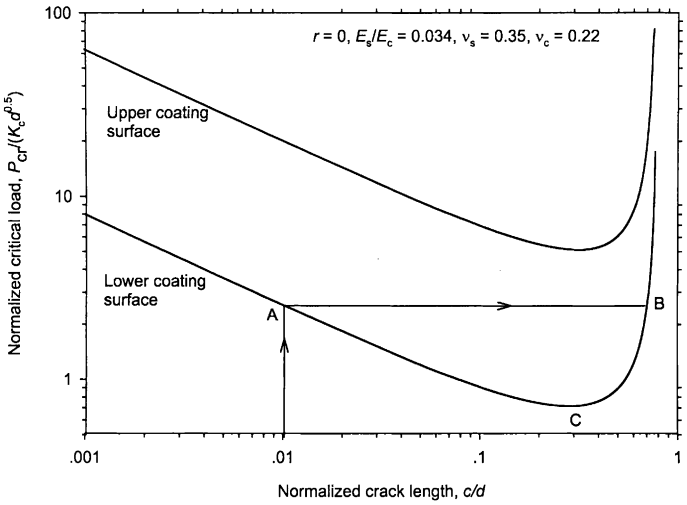

Fig. 10. FEM fracture mechanics predictions for the normalized load needed to initiate cracking in the lower and upper surfaces of the coating as a function of normalized crack length; glass/polycarbonate bi-layer subject to line-loading.

concave, indicating a range of crack length for which unstable growth occurs. Consider, for example, the lower surface crack, with c/d initially set at 0.01. As the loading is increased from zero, one moves along the vertical solid line until point A is reached, at which time crack propagation occurs. The ensuing growth is seen to be unstable, terminating at point B (dynamic effects notwithstanding). Upon increasing the load from that point, the growth becomes stable, but the crack never reaches the top surface. One also observes that if the coating thickness is less than that corresponding to the minimum at point C (i.e., $c/d = 0.3$), the entire growth is stable. As will be shown next, the minimum in the curve is of a special significance when the coating surface contains a population of flaws of various sizes instead of a single crack. Similar behavior is also observed for the upper surface crack, with the minimum again occurring at $c/d = 0.3$.

3.2.4. Consideration of flaw population

In many applications, a distribution of cracks of various sizes, rather than a single crack, may be present on the surfaces of the coating. While in most fracture scenarios failure generally originate from the larger flaw, here, because of the shielding effect provided by the compression stress field ahead of the crack tip under certain conditions failure may actually initiate from small rather than large flaws in the population. This is illustrated in Fig. 11, where the variations of P_{cr} with d from Eqs. (9) and (10) are depicted as upper and lower sets of solid lines, respectively, for three different crack lengths, i.e., 5, 10 and 20 μm. In all cases, $E_s/E_c = 0.034$. As shown, while the largest crack in this set is the detrimental one for large values of d, the smallest one dominates the strength for very thin coatings.

Let a population of cracks ranging in length from zero to c, where c is the largest crack present on the surface of the coating, exists. As discussed in Section 3.2.3, for a given value of d, there exists a certain crack within this population (i.e., point C in Fig. 10) that provides the least fracture resistance. Denote this crack length as b, and let $b = \beta d$, where β is a parameter that can be easily determined for a given modulus ratio E_s/E_c from approximate polynomial solutions as given in Table 2. (For the special case $E_s/E_c = 0.034$, $\beta = 0.3$). Substituting $b = \beta d$ for c in Eqs. (9) and (10), Eqs. (12a) and (13a) below are obtained. The entire solutions is thus given as

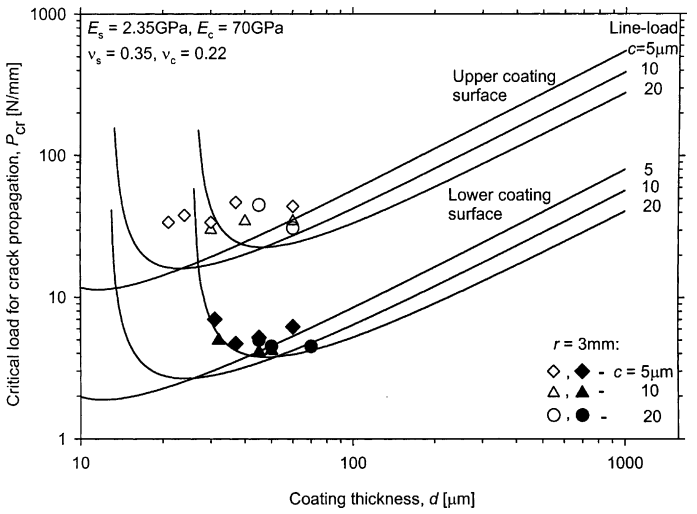

Fig. 11. FEM fracture mechanics predictions for the variations with coating thickness of the load needed to initiate cracking in the lower and upper surfaces of the coating for a glass/polycarbonate system subject to indentation by a steel cylinder; solid lines and symbols correspond to the line-load ($r \to 0$) and the nonlinear ($r = 3$ mm) analyses, respectively. In each case, results are given for 5, 10 and 20 μm long cracks.

Lower coating surface:

$$P_{\mathrm{cr}} = K_{\mathrm{c}} d^{0.5} \Big/ \left[\alpha(\beta) f_{\mathrm{l}} \sqrt{\pi\beta}\right], \quad c/d > \beta \tag{12a}$$

$$P_{\mathrm{cr}} = K_{\mathrm{c}} d \Big/ \left[\alpha f_{\mathrm{l}} \sqrt{\pi c}\right], \quad c/d < \beta \tag{12b}$$

Upper coating surface:

$$P_{\mathrm{cr}} = K_{\mathrm{c}} d^{0.5} \Big/ \left[f_{\mathrm{u}} \sqrt{\pi\beta\{\alpha_1^2(\beta) + \alpha_2^2(\beta)\}}\right], \quad c/d > \beta \tag{13a}$$

$$P_{\mathrm{cr}} = K_{\mathrm{c}} d \Big/ \left[f_{\mathrm{u}} \sqrt{\pi c(\alpha_1^2 + \alpha_2^2)}\right], \quad c/d < \beta \tag{13b}$$

where, as discussed earlier in this work, Eqs. (12b) and (13b) are limited to the range c/d for which no contact between the two crack faces occurs (i.e., $K_{\mathrm{I}} > 0$). Note that the critical loads in Eqs. (12a) and (13a) are proportional to the *square root* of d. These relations are plotted in Fig. 9a and b as straight, dotted lines. The latter are terminated where they meet the solid lines; for larger values of d/c, the associated flaw size would exceed the largest flaw in the population, c. Fig. 9 shows that this consideration drastically reduces the fracture load for very thin coatings, i.e., from unbounded to a finite value.

4. Nonlinear finite element analysis

The behavior for a finite size indenter is evaluated next. The extended contact region that is developed under the indenter induces geometric and possibly material nonlinear effects, especially for very thin coatings. The following FEA is concerned only with the experimental conditions, namely a glass layer bonded to a polycarbonate substrate, the whole of which is indented by a steel cylinder of radius $r = 3$ mm. The contact between the surface of the cylinder and the coating is modeled using a built-in contact algorithm in ANSYS. Plane-strain, large deformation and frictionless contact conditions are invoked in the FEA. A fine mesh is used in those regions where stress concentration occurs. The coating and the substrate are assumed linearly elastic. As for the line-load analysis, we first deal with the uncracked configuration before moving on to consider crack propagation.

4.1. Stress analysis—no crack

The effect of load on the distribution of radial stresses in the coating is shown in Fig. 5 for a relatively thin coating ($d = 20$ μm). The presentation is limited to the coating region, with the contours of negative stress given a relatively low contrast. As the load is increased, the stress concentration on the lower coating surface tends to diffuse, with the location of the peak stress shifting away from the symmetry plane. Also, the compression stress in this region occupies an increasingly larger portion of the coating thickness. As discussed earlier, effect may favor the growth of smaller rather than larger cracks in the flaw population. One also observe from these prints that the distance to the peak stress on the upper coating surface, R_{u}, tend to approach the edge of the contact (identified by the vertical arrows), as the load is increased. Figs. 12 and 13 detail some of these observations quantitatively for a 20 μm and a 30 μm thick coating. In these figures, the isolated symbols and the smooth curves denote FEM data and corresponding fits, respectively. Fig. 12 (dotted lines) shows that the normalized peak radial stress on the lower coating surface is monotonically decreasing as P is increased. This effect, which results from the diffusion of the stress concentration under the expanding contact area, is accentuated with decreasing the coating thickness. The variations with load

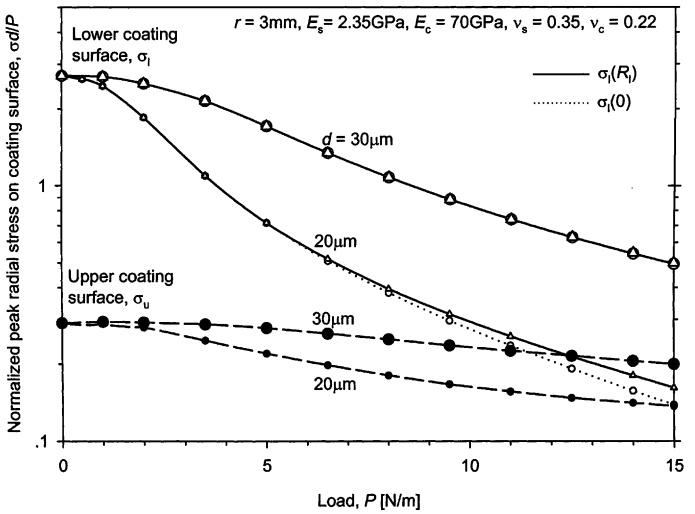

Fig. 12. FEM predictions for the variations with load of the normalized peak radial stress on the lower (open circles) and upper (filled circles) coating surfaces for two glass/polycarbonate bi-layers ($d = 20$ μm and $d = 30$ μm) indented by a steel cylinder of radius $r = 3$ mm. Also shown (triangular symbols) are results for the radial stress at the intersection of the lower coating surface and the symmetry plane (i.e., $R_l = 0$). Curves are smooth fits to the FEM data.

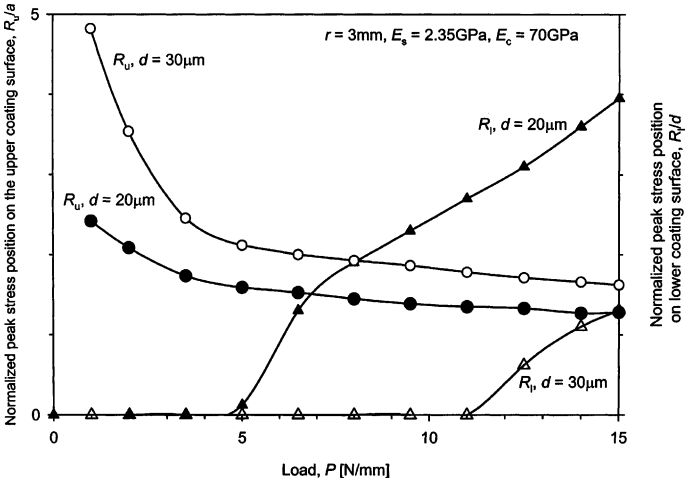

Fig. 13. FEM predictions (symbols) for the variation with load of the normalized position of the peak radial stress on the upper and lower coating surfaces, R_u/a and R_l/d, respectively, where a denotes half the contact length, for two glass/polycarbonate bi-layers ($d = 20$ μm and $d = 30$ μm) indented by a steel cylinder of radius $r = 3$ mm. Curves are smooth fits to the FEM data.

of the normalized peak stress on the upper coating surface (dashed lines in Fig. 12) are much more moderate, attesting to a much lesser shielding effect. In fact, for the thinner coating, the stress on the upper coating thickness exceeds that on the lower surface once P is increased from 15 N/mm. One also observes from this as well as from Fig. 13 that the position of the peak radial stress on the lower coating surface, R_l shifts away from the symmetry axis once the load is increased from 5 N/mm ($d = 20$ μm) or 11 N/mm ($d = 30$ μm). It is apparent from these results that under the conditions that promote relatively large contact area at fracture (e.g., large indenters, tough coatings, stiff substrates), the fracture on the lower

coating surface follows that from the upper surface. Also, the fracture on the lower coating surface would be associated with a series of off-axis cracks, rather than a single, central crack, and the fracture on the upper surface would occur close to the contact edge.

4.2. Crack propagation analysis

The following analysis employs a single crack of length c, extending vertically either from the upper or the lower coating surfaces. The critical load for crack propagation is obtained when the energy release rate, G, given at the right hand side of Eq. (8), reaches its critical value, G_c. For the present soda lime glass coating, $G_c = 6.8$ N/m or, from Eq. (11), $K_c = 0.7$ MPa $m^{1/2}$ (Lawn, 1995). The stress intensity factors K_1 and K_2 are determined with the aid of the FEM crack tip displacements (Eq. (3) or (6)). The crack at the lower coating surface is positioned on the symmetry plane ($R_i = 0$), where, for the present glass/polycarbonate system, the radial stress is maximized. The analysis of the upper surface crack is more involved because the position of the peak radial stress is not known a priori. In this case, FEA are performed for a number of reasonable crack locations, with the least critical load obtained among all such runs taken as the critical load. (Other approaches that have been employed to overcome such difficulty include the use of a *series* of cracks (Souza et al., 2001) or the use of cohesive elements (Abdul-Baqi and Van der Giessen, 2002).)

The presence of a range of flaw sizes rather than a single crack on the abraded coating surface needs a special consideration. Miranda et al. (2001) have studied the flaw distribution on the surface of a glass subject to the same abrasion procedure as used in this study. The results show that the flaws range in size from 0 to about 30 μm. The depth of these cracks, which is the more relevant quantity here, is expected to be somewhat smaller. Thus, judging from the line-load analysis discussed in connection with Fig. 11, the entire range of crack lengths in the flaw population must be treated in order to assess the least load needed to initiate crack propagation. As discussed earlier, for thick coatings the largest flaw in the population dominates the fracture. Because for thick coatings the stresses on the lower and upper coating surfaces are insensitive to the contact details, one may use the line-load results to fit the test data in that range. This is done in Fig. 4, where it is seen that a 23 μm long crack, represented by the thick solid lines, provides a good fit for the two crack systems under consideration once d exceeds several hundred microns. Clearly, this value of c constitutes an upper bound for the flaw distribution. To obtain critical loads for thinner coatings, the full contact analysis (i.e., $r = 3$ mm) must be used. Consider, for this purpose, Fig. 11 again, where the critical loads from the line-load analysis are given as solid line curves for three different crack lengths, i.e., 5, 10 and 20 μm. Also shown in this figure as symbols are the corresponding critical loads obtained from the nonlinear FEA (i.e., $r = 3$ mm). Consider first the lower surface crack, with $c = 20$ μm. As shown, the FEM data in this case (filled circles) tend to coincide with the corresponding line-load results once d is increased from about 100 μm. These data are terminated at 45 μm, however, because for thinner coatings the fracture criterion is never met. (When plotted against P, the energy release rate exhibited a reversal in trend, first rising and then declining, its peak value being less than G_c; this reversal is attributed to the shielding effect induced by the expanding contact area.) Now, when the smaller cracks in this figure are considered, fracture in thinner coatings become possible, albeit with an ever increase load. This process continues up to $d \cong 30$ μm; for thinner coatings, the fracture criterion was never fulfilled regardless of the crack length used. Clearly, for a given coating thickness, the least fracture load obtained among all possible choices of crack lengths would constitute the critical load. The fracture envelope obtained in this way (i.e., a smooth curve joining the lowest data) is depicted in Fig. 4 as a dotted curve. This curve agrees well with the line-load results once d is increased from about 100 μm. Note that this curve is given a very steep rise toward the small thickness end, to highlight the fact that no crack growth is possible for thinner coatings. As shown, the combined predictions from the line-load and the nonlinear analyses seem to agree reasonably well with the available experimental data throughout the coating thickness range used.

The results for the upper surface crack are similarly presented in Fig. 11, with the solid lines and the open symbols corresponding to the line-load and the nonlinear FEM analysis, respectively. The fracture behavior in this case differs from its lower surface counterpart in that crack propagation for very thin coatings is now possible, with the fracture strength remaining nearly fixed with decreasing d. (Note that the data are terminated at $d = 20$ μm, which is the thinnest coating analyzed.) As shown in Fig. 4, the fracture envelope in this case (i.e., the upper dotted curve) intersects its lower surface counterpart at $d \cong 30$ μm. A general conclusion that may be drawn from these observations is that the fracture in ultra thin coatings is dominated by the upper surface crack, especially when large contact areas are involved. The results presented show that the indenter radius plays a major role on the interrelationship between the lower and upper surface crack systems. This issue is addressed in a forthcoming paper in connection with spherical type indentation (Chai, submitted).

4.3. Crack path

The initial deviation in the path of the upper surface crack is considered next. As shown from Fig. 3, following a phase of nearly co-planer or vertical growth, the crack tends to deviate and ultimately propagate parallel to the interface. Of interest here is the direction of that deviation. In brittle fracture, the crack path is generally taken to follow the maximum principal stress trajectory (Erdogan and Sih, 1963):

$$K_1 \sin\theta + K_2(3\cos\theta - 1) = 0 \tag{14}$$

Dividing by K_1 and using Eq. (6), one gets

$$\sin\theta + (u_2/u_1)(3\cos\theta - 1) = 0 \tag{15}$$

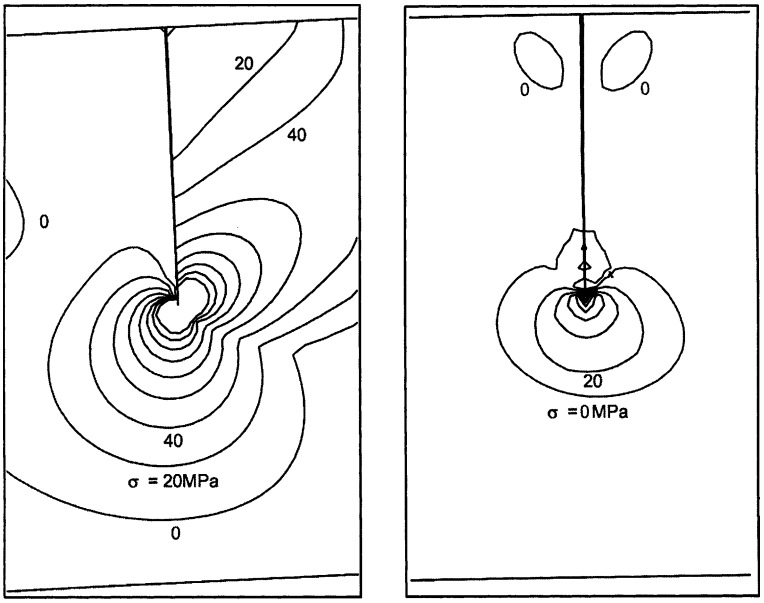

Fig. 14. FEM first principal stress contours for a glass/polycarbonate bi-layer containing a vertical crack of length c equals $0.5d$ that emanates from the upper coating surface; only the coating part is illustrated. Fig. 14a and b simulate the tests shown in Fig. 3a and b, respectively.

where θ is the angle of deviation relative to a co-planar growth, being positive for a crack propagating away from the symmetry plane. FEM analyses were conducted for the two tests depicted in Fig. 3a and b in an attempt to elucidate the cause for the opposing crack propagation directions. The exact conditions for each of these tests were inputted into the analysis. Note that these two tests differ primarily in the ratio R_u/d, which is 3.1 and 4.4 for the case of Fig. 3a and b, respectively. In both the cases, the crack length is taken to be half the coating thickness. Fig. 14 shows FEM contour plots of the first principal stress corresponding to these tests. Fig. 14a shows that the principal stresses are such that cracking would occur away from the symmetry plane, in consistency with the test results (Fig. 3a). In the case of Fig. 14b, no strong directional preference is apparent, which again agree with the behavior in Fig. 3b, where cracking in both directions occurred.

5. Discussions

For very thick coatings (i.e. $c/d \to 0$), the onset of fracture can be alternatively determined by specifying a critical stress, σ^F, value in Eq. (1). One may thus write from this equation

$$P_{crl}/P_{cru} = (f_u/f_l)(\sigma_l^F/\sigma_u^F), \tag{16}$$

where the subscripts "l" and "u" denote lower and upper coating surfaces, respectively. Note that the critical stresses for the upper and lower coating surfaces differ. While σ_u^F can be determined from a relatively simple experiment such as the four-point bending test, the evaluation of σ_l^F requires a more elaborate test where the coating material is bonded to the substrate. This quantity can be established, however, from the FEA. Using Eqs. (12b) and (13b), the ratio of the critical loads associated with the lower and upper coating surfaces can be obtained. Specifying the results to the thick coating regime by imposing $c/d \to 0$, one has

$$P_{crl}/P_{cru} = (f_u/f_l)\sqrt{[\alpha_l^2(0) + \alpha_l^2(0)]/\alpha^2(0)} \tag{17}$$

Comparing Eqs. (16) and (17), one gets

$$\sigma_l^F/\sigma_u^F = \sqrt{[\alpha_l^2(0) + \alpha_l^2(0)]/\alpha^2(0)} \tag{18}$$

The asymptotic values of the correction functions in Eq. (18) are directly obtainable from the coefficients a_0 in Table 2. For the specific case of glass/polycarbonate bi-layer, the results is found to be $\sigma_l^F/\sigma_u^F = 1.36$. Introducing this ratio in Eq. (16), taking $f_l = 2.75$ and $f_u = 0.29$ (Fig. 6), one gets $P_{crl}/P_{cru} = 0.143$. This compares favorably with the experimental ratio of 1.33 that can be easily inferred from the test results in Fig. 4. Note that the assumption $\sigma_l^F/\sigma_u^F = 1$ leads to a ratio P_{crl}/P_{cru} of 0.105, which is way beyond the experimental results.

6. Summary and conclusions

The fracture resistance of bi-layer structures consisting of a hard coating bonded to a thick and compliant substrate, the whole of which is indented by a 3 mm radius steel cylinder, is investigated. The bending of the cover layer under the softer substrate induces two sets of concentrated tensile stress region in the coating, one on the lower surface and the other on the top surface of the coating, a distance from the edge of the contact area. The evolution of damage from these sites is observed in-situ for a range of coating thickness using a model transparent glass/polycarbonate bi-layer system. The critical load for crack propagation for thick coatings is nearly ten times larger for the upper surface crack as compared to the lower surface crack. These quantities increased linearly with the coating thickness except for thin coatings, where an interesting reversal in trends occurs. This behavior is much similar to that for the axisymmetric analogue case (Chai et al., 1999), albeit with a proportionality of P_{cr} to d instead of d^2 in the limit $d/c \gg 1$.

A fracture mechanics analysis in conjunction with FEM is performed to elucidate the critical loads for crack propagation. Cracks are assumed to emanate vertically either from the lower coating surface, directly under the indenter, or from the upper coating surface, a distance from the symmetry plane. Fracture is assumed when the total energy release rate reaches a critical value. Because the position of the crack on the upper coating surface is not known in advance, analyses are performed for a number of reasonable locations, with the least critical load obtained among these analyses taken as the true fracture load. The analysis also considers the case where a *range* of flaw size, rather than a single crack, is present on the coating surfaces. In this case, the above procedure needs to be repeated over the entire range of flaws present. In this work, a few reasonable crack sizes are considered. The fracture resistance obtained from this analysis is greatly dependent on the coating thickness. For thick coatings, the critical load in each crack system is proportional to d. For relatively thin coatings, a major change from this trend occur, the cause of which is attributed to compression stresses that are generated ahead of the crack tip. This effect, which is particularly pronounced for the lower surface crack, tends to shield the crack or increase the fracture resistance. The specific behavior in this thickness range is dictated by a complex interplay between the contact area, the coating thickness and the crack length. An additional factor in this scheme is flaw distribution, where small flaws may become more detrimental than large ones. For our case study of glass/polycarbonate bi-layer with $r = 3$ mm, the fracture resistance associated with the lower coating surface actually increases once d is decreased from about 50 μm. Moreover, for coatings thinner than 30 μm, this type of cracking is completely suppressed, irrespective of the flaw size used. In the case of the upper surface crack, the fracture resistance is quite fixed once d is decreased from about 50 μm. The results of the FEM analysis are in quantitative agreement with the tests.

The case of line-load ($r \to 0$) is of special interest because it provides *lower bounds* for the critical loads, and furthermore the analysis becomes linearly elastic. For relatively thin coatings, the critical loads for both crack systems tend to approach infinity as the coating thickness become comparable to the crack length. When flaw distribution is considered, the critical loads for thin coatings becomes finite, e.g., proportional to $d^{0.5}$. Comparison of the line-load and the nonlinear analysis reveals the importance of the indenter radius. Decreasing the latter reduces the fracture strength. The closed-form approximate solutions for the critical loads obtained for the line-load analysis may serve as a useful guide for conservative design.

The major entity controlling the fracture resistance of the coating appears to be the ratio of contact size to coating thickness. For a given coating thickness, the contact size at fracture increases with increasing the either the indenter radius, the toughness of the coating or the stiffness of the substrate. In applications where these parameters are relatively large, the failure from the upper coating surface appears to be the detrimental strength factor, with the crack tending to occur close to the edge of the contact. These results seem to be in general agreement with spherical indentation tests associated with ultra thin coatings.

Beyond direct applications, cylindrical type indentation may facilitate a simplified mean for studying the more common but analytically more complex case of spherical indentation. This is particularly true for the damage associated with the lower coating surface, where the fracture is reduced from a 3-D to a 2-D configuration. Testing under plane-strain conditions also allows for characterizing thin-film fracture and assessing thin-film toughness in opaque materials through observations from the specimen edge. The relatively simple line-load analysis may be especially useful in this context. At this stage of the experimentation, implementation of this approach to very thin coatings is not straightforward.

References

Abdul-Baqi, A., Van der Giessen, E., 2002. Numerical analysis of indentation-induced cracking of brittle coatings on ductile substrates. International Journal of Solids and Structures 39, 1427–1442.

Benabdallah, H.S., Boros, I.E., 1996. Finite element analysis of the indentation of thick coatings by a cylindrical indenter. Transactions of the CSME 20, 217–232.

Chai, H., Lawn, B.R., Wuttiphan, S., 1999. Fracture modes in brittle coatings with large interlayer modulus mismatch. Journal of Material Research 14, 3805–3817.

Chai, H., submitted. Fracture mechanics analysis of thin coatings under spherical indentation. International Journal of Fracture (submitted).

Diao, D.F., Kato, K., Hokkirigawa, K., 1994. Fracture mechanism of ceramic coatings in indentation. Journal of Tribology 116, 860–869.

Elsharkawy, A.A., 1999. Effect of friction on subsurface stresses in sliding line contact of multilayered elastic solids. International Journal of Solids and Structures 36, 3903–3915.

Erdogan, F., Sih, G.C., 1963. On the crack extension in plates under plane loading and transverse shear. Journal of Basic Engineering 85, 519–527.

Ewalds, H.L., Wanhill, R.J.H., 1986. Fracture Mechanics. Edward Arnold Publishers.

Gecit, M.R., 1979. Fracture of a surface layer bonded to a half space. International Journal of Engineering Science 17, 287–295.

Gilpin, C.B., Haubold, A.D., Ely, J.L., 1996. Finite element analysis of indentation tests on pyrolytic carbon. The Journal of Heart Valve Disease (suppl. I.), S72–S78.

Goryacheva, I., Sadeghi, F., 1995. Contact characteristics of a rolling/sliding cylinder and a viscoelastic layer bonded to an elastic substrate. Wear 184, 125–132.

Johnson, K.L., 1996. Contact Mechanics. Cambridge University Press.

Lardner, J.L., Ritter, J.E., Zhu, G.-Q., 1997. Spherical indentation and fracture of glass plates. Journal of the American Ceramic Society 80, 1851–1862.

Lawn, B.R., 1995. Fracture of Brittle Solids, 2nd ed. Cambridge University Press.

Lawn, B.R., Lee, K.S., Chai, H., Pajares, A., Kim, D.K., Wuttiphan, S., Peterson, I.M., Hu, X., 2000. Damage-resistance brittle coatings. Advanced Engineering Materials 2, 745–748.

Mahajan, P., 1998. Contact behavior of an orthotropic laminated beam indented by a rigid cylinder. Composites Science and Technology 58, 505–513.

Michler, J., Tobler, M., Blank, E., 1999. Thermal annealing behavior of alloyed DLC films on steel: determination and modeling of mechanical properties. Diamond and Related Materials 8, 510–516.

Miranda, P., Pajares, A., Guiberteau, F., Cumbrera, F.L., Lawn, B.R., 2001. Role of flaw statistics in contact fracture of brittle coatings. Acta Materialia 49, 3719–3726.

Rhee, Y.-W., Kim, H.-W., Deng, Y., Lawn, B.R., 2001. Fracture of ceramic coatings on compliant substrates: design considerations. Journal of the American Ceramic Society 18, 1066.

Souza, R.M., Sinatora, A., Mustoe, G.G.W., Moore, J.J., 2001. Numerical and experimental study of the circular cracks observed at the contact edges of the indentations of coated systems with soft substrates. Wear 251, 1337–1346.

Wang, J.S., Sugimura, Y., Evans, A.G., Tredaway, W.K., 1998. The mechanical performance of DLC films on steel. Thin Solid Films 325, 163–174.

Weppelmann, E., Swain, M.V., 1996. Investigation of stresses and stress intensity factors responsible for fracture of thin protective films during ultra-micro indentation tests with spherical indenters. Thin Solid Films 286, 111–121.

Yuan, F., Hayashi, K., 1999. Influence of the grain size of the alumina coating on crack initiation in indentation. Wear 225–229, 83–89.